Non-Linear Anisotropic Elasticity for Real-Time Surgery Simulation

Guillaume Picinbono, Hervé Delingette, Nicholas Ayache

INRIA

INSTITUT NATIONAL DE RECHERCHE EN INFORMATIQUE ET EN AUTOMATIQUE

Non-Linear Anisotropic Elasticity for Real-Time Surgery Simulation

Guillaume Picinbono — Hervé Delingette — Nicholas Ayache

N° 4028

Octobre 2000

THÈME 3

ISSN 0249-6399 ISRN INRIA/RR--4028--FR+ENG

INRIA
SOPHIA ANTIPOLIS

Non-Linear Anisotropic Elasticity for Real-Time Surgery Simulation

Guillaume Picinbono , Hervé Delingette , Nicholas Ayache

Thème 3 — Interaction homme-machine,
images, données, connaissances
Projet Epidaure

Rapport de recherche n° 4028 — Octobre 2000 — 21 pages

Abstract: In this article, we describe the latest developments of the minimally invasive hepatic surgery simulator prototype developed at INRIA. A key problem with such a simulator is the physical modeling of soft tissues. We propose a new deformable model based on non-linear elasticity, anisotropic behavior, and the finite element method. This model is valid for large displacements, which means in particular that it is invariant with respect to rotations. This property improves the realism of the deformations and solves the problems related to the shortcomings of linear elasticity, which is only valid for small displacements. We also address the problem of volume variations by adding to our model incompressibility constraints. Finally, we demonstrate the relevance of this approach for the real-time simulation of laparoscopic surgical gestures on the liver.

Key-words: Surgery simulation, non-linear elasticity, large displacement, finite element method, deformable model, real-time, anisotropy, incompressibility constraints.

Unité de recherche INRIA Sophia Antipolis
2004, route des Lucioles, B.P. 93, 06902 Sophia Antipolis Cedex (France)
Téléphone : 04 92 38 77 77 - International : +33 4 92 38 77 77 —Fax : 04 92 38 77 65 - International : +33 4 92 38 77 65

Élasticité non-linéaire anisotrope pour la simulation de chirurgie en temps réel

Résumé : Dans cet article, nous décrivons les derniers développements du prototype de simulateur de chirurgie minimalement invasive sur le foie développé à l'INRIA. Un problème clé avec ce genre de simulateur est la modélisation physique des tissus mous. Nous proposons un nouveau modèle déformable basé sur l'élasticité non-linéaire, le comportement anisotrope, et la méthode des éléments finis. Ce modèle reste valable pour les grands déplacements, ce qui signifie en particulier qu'il est invariant par rotation. Cette propriété améliore le réalisme des déformations et résout les problèmes liés aux limitations de l'élasticité linéaire, qui n'est valable que pour les petits déplacements. Nous nous intéressons aussi au problème de la variation de volume en ajoutant à notre modèle des contraintes d'incompressibilité. Enfin, nous démontrons le bien-fondé de cette approche pour la simulation en temps réel de gestes chirurgicaux en laparoscopie sur le foie.

Mots-clés : Simulation de chirurgie, élasticité non-linéaire, grands déplacements, méthode des éléments finis, temps réel, anisotropie, contraintes d'incompressibilité.

Contents

1 Introduction **4**

2 Shortcomings of the linear elasticity model **4**
2.1 Finite element method 5
2.2 The problem of rotational invariance 6

3 St Venant-Kirchhoff elasticity **7**
3.1 Finite element modeling 8
3.2 Non-linear Tensor-Mass Model 9

4 Incompressibility constraint **11**

5 Results **12**

6 Optimization of non-linear deformations **15**

7 Validation **17**

8 Conclusion **18**

A Update operations when removing a tetrahedron from the mesh **18**

B Non-linear force equation **18**

1 Introduction

A major and recent evolution in abdominal surgery has been the development of laparoscopic surgery. In this type of surgery, abdominal operations such as hepatic resection are performed through small incisions. A video camera and special surgical tools are introduced into the abdomen, allowing the surgeon to perform a procedure less invasive. A drawback of this technique lies essentially in the need for more complex gestures and in the loss of direct visual and tactile information. Therefore the surgeon needs to learn and adapt himself to this new type of surgery and in particular to a new type of hand-eye coordination. In this context, surgical simulation systems could be of great help in the training process of surgeons.

Among the several key problems in the development of a surgical simulator [1, 15], the geometrical and physical representation of human organs remain the most important. The deformable model must be at the same time very realistic (both visually and physically) and very efficient to allow real-time deformations. Several methods have been proposed: spring-mass models [10, 14], free form deformations [2], linear elasticity with finite volume method [11] or various finite element methods [7, 12, 17, 4, 20, 19].

In this article we propose a new real-time deformable model based on non-linear elasticity and a finite element method. We first introduce the linear elasticity theory and its implementation through the finite element method, and we then highlight its shortcomings when the "small displacement" hypothesis does not hold. Then we focus on our implementation of St Venant-Kirchhoff elasticity and incompressibility constraints.

2 Shortcomings of the linear elasticity model

Linear elasticity is often used for the modeling of deformable materials, mainly because the equations remain quite simple and the computation time can be optimized.

The physical behavior of soft tissue may be considered as linear elastic if its displacement and deformation remain small [13, 16] (typically less than 10% of the mesh size). We represent the deformation of a volumetric model from its rest shape $\mathcal{M}_{\text{initial}}$ with a *displacement vector* $\mathbf{U}(x,y,z)$ for $(x,y,z) \in \mathcal{M}_{\text{initial}}$ and we write $\mathcal{M}_{\text{deformed}} = \mathcal{M}_{\text{initial}} + \mathbf{U}(x,y,z)$. From this displacement vector, we define the linearized *Green-St Venant strain tensor* (3×3 symmetric matrix) E_l and its principal invariants l_1 and l_2:

$$E_l = \frac{1}{2}\left(\nabla \mathbf{U} + \nabla \mathbf{U}^t\right) \qquad l_1 = tr\ E_l \qquad l_2 = tr\ {E_l}^2. \tag{1}$$

The linear elastic energy W_{Linear}, for homogeneous isotropic materials, is defined by the following formula (see [6]):

$$\begin{aligned} W_{Linear} &= \frac{\lambda}{2}\,(trE_l)^2 + \mu\ tr{E_l}^2 \\ &= \frac{\lambda}{2}(div\ \mathbf{U})^2 + \mu\|\nabla \mathbf{U}\|^2 - \frac{\mu}{2}\|rot\ \mathbf{U}\|^2, \end{aligned} \tag{2}$$

where λ and μ are the *Lamé coefficients* characterizing the material stiffness.

Equation 2, known as *Hooke's law*, shows that the elastic energy of a deformable object is a quadratic function of the displacement vector.

2.1 Finite element method

Finite element method is a classical way to solve continuum mechanics equations. It is a mathematical framework to discretize a continuous variational problem [22]. We chose to use P_1 finite elements where the elementary volume is a tetrahedron with a node defined at each vertex. At each point $\mathbf{M}(x,y,z)$ inside tetrahedron $\mathbf{T}_i$, the displacement vector is expressed as a function of the displacements $\mathbf{U}_k$ of vertices $\mathbf{P}_k$. For P_1 finite elements, interpolation functions $\mathbf{\Lambda}_k$ are linear ($\{\mathbf{\Lambda}_k; k=0,...,3\}$ are the barycentric coordinates of $\mathbf{M}$ in the tetrahedron):

$$\mathbf{U}(x,y,z) = \sum_{j=0}^{3} \mathbf{U}_j \Lambda_j(x,y,z) \qquad \mathbf{\Lambda}_j(x,y,z) = \boldsymbol{\alpha}_j.X + \boldsymbol{\beta}_j$$

$$\boldsymbol{\alpha}_j = \frac{(-1)^j}{6V(\mathbf{T}_i)}(\mathbf{P}_{j+1} \times \mathbf{P}_{j+2} + \mathbf{P}_{j+2} \times \mathbf{P}_{j+3} + \mathbf{P}_{j+3} \times \mathbf{P}_{j+1}),$$

where $\times$ stands for the cross product between two vectors, and $V(\mathbf{T}_i)$ is the volume of the tetrahedron.

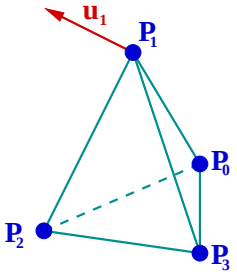

Figure 1: P_1 *finite element*

Using this equation for the displacement vector $\mathbf{U}$ leads to the finite element formulation of linear elastic energy in the tetrahedron $\mathbf{T}_i$ [12]:

$$\begin{aligned} W_{Linear}(\mathbf{T}_i) &= \sum_{j,k=0}^{3} \mathbf{U}_j^t [\mathcal{B}_{jk}^{\mathbf{T}_i}] \mathbf{U}_k \\ \mathcal{B}_{jk}^{\mathbf{T}_i} &= \frac{\lambda}{2}(\boldsymbol{\alpha}_j \otimes \boldsymbol{\alpha}_k) + \frac{\mu}{2}\left[(\boldsymbol{\alpha}_k \otimes \boldsymbol{\alpha}_j) + (\boldsymbol{\alpha}_j.\boldsymbol{\alpha}_k)\, Id_3\right], \end{aligned} \tag{3}$$

where $[\mathcal{B}_{jk}^{\mathbf{T}_i}]$ is the tetrahedron contribution to the stiffness tensor of the edge $(\mathbf{P}_j, \mathbf{P}_k)$ (or of the vertex $\mathbf{P}_j$ if $j=k$), $\{\boldsymbol{\alpha}_j, k=0,..,3\}$ are the shape vectors of the tetrahedron and $\otimes$ stands for the tensor product of two vectors, which gives a (3x3) matrix: $\mathbf{u} \otimes \mathbf{v} = \mathbf{u}\,\mathbf{v}^t$. Id_3 is the (3x3) identity matrix.

Finally, to obtain the force $\mathbf{F}_p^{\mathbf{T}_i}$ applied by the tetrahedron $\mathbf{T}_i$ on the vertex $\mathbf{P}_p$, we derive the elastic energy with respect to the vertex displacement $\mathbf{U}_p$:

$$\mathbf{F}_p^{\mathbf{T}_i} = 2\sum_{j=0}^{3} [\mathcal{B}_{pj}^{\mathbf{T}_i}] \mathbf{U}_j. \tag{4}$$

We have been using this linear elasticity formulation for several years through two deformable models, the **pre-computed model** [7] and the **tensor-mass model** [12, 8]. Furthermore, it can be extended to anisotropic linear elasticity [17, 18], which allows to model fiber-reinforced materials, very common within biological tissues (tendons, muscles, ...), or other anatomical structures like blood vessels.

2.2 The problem of rotational invariance

The main limitation of the linear model is that it is not invariant with respect to rotations. When the object undergoes a rotation, the elastic energy increases, leading to a variation of the volume (see figure 2). In the case of a global rotation of the object, we could solve the problem with a specific change of the reference frame.

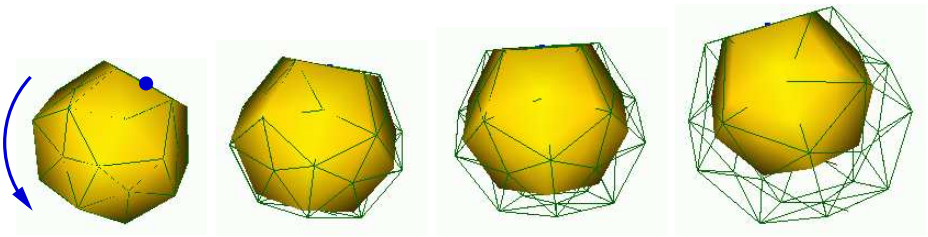

Figure 2: *Global rotation of the linear elastic model (wire-frame)*

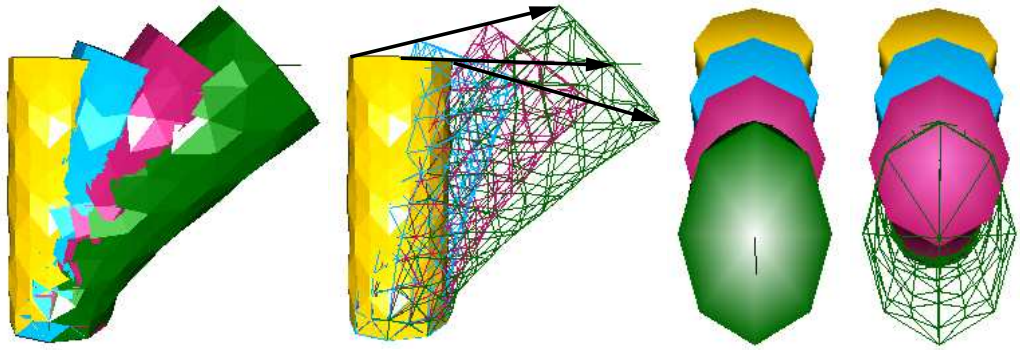

(a) (b) (c) (d)

Figure 3: *Successive deformations of a linear elastic cylinder. (a) and (b): side view. (c) and (d): top view*

But this solution proves itself to be ineffective when only one part of the object undergoes a rotation (which is the case in general). This case is presented by the cylinder of figure 3: the bottom face is fixed and a force is applied to the central top vertex. Arrows show the trajectory of some vertices, which are constrained by the linear model to move along straight lines. This results in the distortion of the mesh. Furthermore, this abnormal deformation is not the same in all directions since the object only deforms itself in the rotation plane (figure 3(c) and 3(d)).

This unrealistic behaviour of the linear elastic model for large displacements led us to consider different models of elasticity.

3 St Venant-Kirchhoff elasticity

A model of elasticity is considered as a large displacement model if it derives from a strain tensor which is a quadratic function of the deformation gradient. Most common tensors are the **left** and **right Cauchy-Green strain tensors** (respectively $B = \nabla\phi\nabla\phi^t$ and $C = \nabla\phi^t\nabla\phi$, ϕ being the deformation function).

The St Venant-Kirchhoff model is a generalization of the linear model for large displacements, and is a particular case of hyperelastic materials. The basic energy equation is the same (equation 2), but now E stands for the complete **Green-St Venant strain tensor**:

$$E = \frac{1}{2}(C - I) = \frac{1}{2}\left(\nabla\mathbf{U} + \nabla\mathbf{U}^t + \nabla\mathbf{U}^t\nabla\mathbf{U}\right). \tag{5}$$

Elastic energy, which was a quadratic function of $\nabla\mathbf{U}$ in the linear case, is now a polynomial of order four with respect to $\nabla\mathbf{U}$:

$$\begin{aligned} W &= \frac{\lambda}{2}\,(trE)^2 + \mu\; trE^2 \\ &= \frac{\lambda}{2}\left[(div\ \mathbf{U}) + \frac{1}{2}\|\nabla\mathbf{U}\|^2\right]^2 + \mu\ \|\nabla\mathbf{U}\|^2 - \frac{\mu}{2}\ \|rot\ \mathbf{U}\|^2 \\ &+ \mu(\nabla\mathbf{U} : \nabla\mathbf{U}^t\nabla\mathbf{U}) + \frac{\mu}{4}\|\nabla\mathbf{U}^t\nabla\mathbf{U}\|^2 \\ W &= W_{Linear} + \frac{\lambda}{2}\,(div\ \mathbf{U})\|\nabla\mathbf{U}\|^2 + \frac{\lambda}{8}\ \|\nabla\mathbf{U}\|^4 \\ &\qquad + \mu\ (\nabla\mathbf{U} : \nabla\mathbf{U}^t\nabla\mathbf{U}) + \frac{\mu}{4}\ \|\nabla\mathbf{U}^t\nabla\mathbf{U}\|^2, \end{aligned} \tag{6}$$

where W_{Linear} is given by equation 2, and $A : B = tr(A^tB) = \sum_{i,j} a_{ij}\ b_{ij}$ is the dot product of two matrices.

In [17, 18], we have generalized linear elasticity to materials having a different behavior in one given direction. These materials, called "transversally isotropic" materials, can also be modeled with St Venant-Kirchhoff elasticity by adding to the isotropic elastic energy of equation 6, an anisotropic contribution which penalizes the material stretch in the direction

given by unit vector $\mathbf{a}_0$:

$$W_{\text{Trans\_iso}} = W + \left(\frac{\lambda^L - \lambda}{2} + \mu^L - \mu\right)\left(\mathbf{a}_0{}^t\, E\, \mathbf{a}_0\right)^2,$$

where λ^L and μ^L are the Lamé constants along the direction of anisotropy $\mathbf{a}_0$.

3.1 Finite element modeling

With the notations introduced in section 2.1, we express the St Venant-Kirchhoff elastic model with finite element theory as:

$$\begin{aligned} W(\mathbf{T}_i) &= \sum_{j,k} \mathbf{U}_j^t \left[\mathcal{B}_{jk}^{\mathbf{T}_i}\right] \mathbf{U}_k + \sum_{j,k,l} \left(\mathbf{U}_j.\mathcal{C}_{jkl}^{\mathbf{T}_i}\right)(\mathbf{U}_k.\mathbf{U}_l) \\ &+ \sum_{j,k,l,m} \mathcal{D}_{jklm}^{\mathbf{T}_i}\,(\mathbf{U}_j.\mathbf{U}_k)\,(\mathbf{U}_l.\mathbf{U}_m)\,, \end{aligned} \tag{8}$$

where the terms $\mathcal{B}_{jk}^{\mathbf{T}_i}$, $\mathcal{C}_{jkl}^{\mathbf{T}_i}$, and $\mathcal{D}_{jklm}^{\mathbf{T}_i}$, called "stiffness parameters", are given by:

- $\mathcal{B}_{jk}^{\mathbf{T}_i}$ is a (3x3) symmetric matrix (which corresponds to the linear component of the energy):

$$\begin{aligned} \mathcal{B}_{jk}^{\mathbf{T}_i} &= \frac{\lambda}{2}\,(\boldsymbol{\alpha}_j \otimes \boldsymbol{\alpha}_k) + \frac{\mu}{2}\,[(\boldsymbol{\alpha}_k \otimes \boldsymbol{\alpha}_j) + (\boldsymbol{\alpha}_j.\boldsymbol{\alpha}_k)\,Id_3] \\ &+ \left(\frac{\lambda^L - \lambda}{2} + \mu^L - \mu\right)(\mathbf{a}_0 \otimes \mathbf{a}_0)(\boldsymbol{\alpha}_j \otimes \boldsymbol{\alpha}_k)(\mathbf{a}_0 \otimes \mathbf{a}_0), \end{aligned}$$

- $\mathcal{C}_{jkl}^{\mathbf{T}_i}$ is a vector:

$$\begin{aligned} \mathcal{C}_{jkl}^{\mathbf{T}_i} &= \frac{\lambda}{2}\boldsymbol{\alpha}_j\,(\boldsymbol{\alpha}_k.\boldsymbol{\alpha}_l) + \frac{\mu}{2}\,[\boldsymbol{\alpha}_l\,(\boldsymbol{\alpha}_j.\boldsymbol{\alpha}_k) + \boldsymbol{\alpha}_k\,(\boldsymbol{\alpha}_j.\boldsymbol{\alpha}_l)] \\ &+ \left(\frac{\lambda^L - \lambda}{2} + \mu^L - \mu\right)(\mathbf{a}_0 \otimes \mathbf{a}_0)(\boldsymbol{\alpha}_j \otimes \boldsymbol{\alpha}_k)(\mathbf{a}_0 \otimes \mathbf{a}_0)\boldsymbol{\alpha}_l, \end{aligned}$$

- and $\mathcal{D}_{jklm}^{\mathbf{T}_i}$ is a scalar:

$$\begin{aligned} \mathcal{D}_{jklm}^{\mathbf{T}_i} &= \frac{\lambda}{8}\,(\boldsymbol{\alpha}_j.\boldsymbol{\alpha}_k)\,(\boldsymbol{\alpha}_l.\boldsymbol{\alpha}_m) + \frac{\mu}{4}(\boldsymbol{\alpha}_j.\boldsymbol{\alpha}_m)(\boldsymbol{\alpha}_k.\boldsymbol{\alpha}_l) \\ &+ \left(\frac{\lambda^L - \lambda}{8} + \frac{\mu^L - \mu}{4}\right)(\mathbf{a}_0.\boldsymbol{\alpha}_j)(\mathbf{a}_0.\boldsymbol{\alpha}_k)(\mathbf{a}_0.\boldsymbol{\alpha}_l)(\mathbf{a}_0.\boldsymbol{\alpha}_m). \end{aligned}$$

- The last term of each stiffness parameter represents the anisotropic behavior of the material.

The force applied at each vertex $\mathbf{P}_p$ inside a tetrahedron is obtained by derivation of the elastic energy $W(\mathbf{T}_i)$ with respect to the displacement $\mathbf{U}_p$:

$$\begin{aligned}\mathbf{F}^p(\mathbf{T}_i) &= \underbrace{2\sum_j \left[\mathcal{B}_{pj}^{\mathbf{T}_i}\right]\mathbf{U}_j}_{\mathbf{F}_1^p(\mathbf{T}_i)} + \underbrace{\sum_{j,k} 2\left(\mathbf{U}_k \otimes \mathbf{U}_j\right)\mathcal{C}_{jkp}^{\mathbf{T}_i} + \left(\mathbf{U}_j.\mathbf{U}_k\right)\mathcal{C}_{pjk}^{\mathbf{T}_i}}_{\mathbf{F}_2^p(\mathbf{T}_i)} \\ &+ \underbrace{4\sum_{j,k,l} \mathcal{D}_{jklp}^{\mathbf{T}_i}\,\mathbf{U}_l\,\mathbf{U}_k^t\,\mathbf{U}_j}_{\mathbf{F}_3^p(\mathbf{T}_i)}.\end{aligned} \tag{9}$$

The first term of the elastic force ($\mathbf{F}_1^p(\mathbf{T}_i)$) corresponds to the linear elastic case presented in section 2.1. The next part of the article deals with the generalization of the tensor-mass model to large displacements.

3.2 Non-linear Tensor-Mass Model

The main idea of the tensor-mass model is to split, for each tetrahedron, the force applied to a vertex in two parts: a force created by the vertex displacement and forces produced by the displacements of its neighbours:

$$\mathbf{F}_1^p(\mathbf{T}_i) = 2[\mathcal{B}_{pp}^{\mathbf{T}_i}]\mathbf{U}_p + 2\sum_{j\neq p}[\mathcal{B}_{pj}^{\mathbf{T}_i}]\mathbf{U}_j. \tag{10}$$

This way we can define for each tetrahedron a set of **local stiffness tensors** for vertices ($\{\mathcal{B}_{pp}^{\mathbf{T}_i}; p = 0, ..., 3\}$) and for edges ($\{\mathcal{B}_{pj}^{\mathbf{T}_i}; p, j = 0, ..., 3; p \neq j\}$). By doing this for every tetrahedron, we can accumulate on vertices and edges of the mesh the corresponding contributions to the **global stiffness tensors**:

$$\mathcal{B}^{pp} = \sum_{\mathbf{T}_i \in N(\mathbf{V}_p)} \mathcal{B}_{pp}^{\mathbf{T}_i} \qquad\qquad \mathcal{B}^{pj} = \sum_{\mathbf{T}_i \in N(\mathbf{E}_{pj})} \mathcal{B}_{kl}^{\mathbf{T}_i}.$$

These **stiffness tensors** are computed when creating the mesh and are stored for each vertex and edge of the mesh.

The same principle can be applied to the quadratic term ($\mathbf{F}_2^p(\mathbf{T}_i)$ of equation 9) and the cubic term ($\mathbf{F}_3^p(\mathbf{T}_i)$) (see appendix B). The former brings **stiffness vectors** for vertices, edges, and triangles, and the latter brings **stiffness scalars** for vertices, edges, triangles, and tetrahedra. Table 1 summarizes the stiffness parameters stored on each geometrical primitive of the mesh.

Given a tetrahedral mesh of a solid —in our case an anatomical structure— we build a data structure incorporating the notion of vertices, edges, triangles, and tetrahedra, with

Stiffness parameters distribution	Tensors	Vectors	Scalars
Vertex $\mathbf{V}_p$	$\mathcal{B}^{pp}$	$\mathcal{C}^{ppp}$	$\mathcal{D}^{pppp}$
Edge $\mathbf{E}_{pj}$	$\mathcal{B}^{pj}$	$\mathcal{C}^{ppj}$ $\mathcal{C}^{jpp}$ $\mathcal{C}^{jjp}$ $\mathcal{C}^{pjj}$	$\mathcal{D}^{jppp}$ $\mathcal{D}^{jjjp}$ $\mathcal{D}^{jpjp}$ $\mathcal{D}^{pjjp}$ $\mathcal{D}^{jjpp}$
Triangle $\mathbf{F}_{pjk}$		$\mathcal{C}^{jkp}$ $\mathcal{C}^{kjp}$ $\mathcal{C}^{pjk}$	$\mathcal{D}^{jkpp}$ $\mathcal{D}^{jpkp}$ $\mathcal{D}^{pjkp}$ $\mathcal{D}^{jjkp}$ $\mathcal{D}^{jkjp}$ $\mathcal{D}^{kjjp}$ $\mathcal{D}^{kkjp}$ $\mathcal{D}^{kjkp}$ $\mathcal{D}^{jkkp}$
Tetrahedron $\mathbf{T}_{pjkl}$			$\mathcal{D}^{jklp}$ $\mathcal{D}^{jlkp}$ $\mathcal{D}^{kjlp}$ $\mathcal{D}^{kljp}$ $\mathcal{D}^{ljkp}$ $\mathcal{D}^{lkjp}$

Table 1: *Storage of the stiffness parameters on the mesh*

all the necessary neighbours. For each vertex, we store its current position $\mathbf{P}_p$, its rest position $\mathbf{P}_p^0$, and its stiffness parameters. For each edge and each triangle, we store stiffness parameters. Finally for each tetrahedron, we store the Lamé coefficients λ and μ (and λ^L, μ^L, and $\mathbf{a}_0$ if the model is anisotropic), the four shape vectors $\boldsymbol{\alpha}_k$, and the stiffness parameters.

During the simulation, we compute forces for each vertex, edge, triangle, and tetrahedron, and we use a Newtonian differential equation to update the vertex positions:

$$m_i \frac{d^2\mathbf{P}_i}{dt^2} = \gamma_i \frac{d\mathbf{P}_i}{dt} + \mathbf{F}_i \tag{11}$$

This equation is related to the differential equations of continuum mechanics [3]:

$$\mathbf{M}\ddot{\mathbf{U}} + \mathbf{C}\dot{\mathbf{U}} + \mathbf{F}(\mathbf{U}) = \mathbf{R}. \tag{12}$$

Following finite element theory, the mass $\mathbf{M}$ and damping $\mathbf{C}$ matrices are sparse matrices which are related to the stored physical properties of each tetrahedron. In our case, we consider that $\mathbf{M}$ and $\mathbf{C}$ are diagonal matrices, i.e., that mass and damping effects are concentrated at vertices. This simplification called *mass-lumping* decouples the motion of

all nodes and therefore allows us to write equation 12 as the set of independent differential equations for each vertex.

Furthermore, we choose an *explicit integration scheme* where the elastic force is estimated at time t in order to compute the vertex position at time $t+1$:

$$\left(\frac{m_i}{\Delta t^2} - \frac{\gamma_i}{2\Delta t}\right)\mathbf{P}_i^{t+1} = \mathbf{F}_i + \frac{2m_i}{\Delta t^2}\mathbf{P}_i^t - \left(\frac{m_i}{\Delta t^2} + \frac{\gamma_i}{2\Delta t}\right)\mathbf{P}_i^{t-1}.$$

One of the basic tasks in surgery simulation consists in cutting soft tissue. With our deformable model, this task can be achieved efficiently. We simulate the action of an electric scalpel on soft tissue by successively removing tetrahedra at places where the instrument is in contact with the anatomical model.

When removing a tetrahedron, 280 floating numbers update operations are performed to suppress the tetrahedron contributions to the stiffness parameters of the surrounding vertices, edges, and triangles (see appendix A). By locally updating stiffness parameters, the tissue has exactly the same properties as if we had removed the corresponding tetrahedron at its rest position. Because of the volumetric continuity of finite element modeling, the tissue deformation remains realistic during the cutting.

4 Incompressibility constraint

Living tissue, which is essentially made of water, is nearly incompressible. This property is difficult to model and leads in most cases to instability problems. This is the case with the St Venant-Kirchhoff model: the material remains incompressible when the Lamé constant λ tends towards infinity. Taking a large value for λ would force us to decrease the time step and therefore to increase the computation time. Another reason to add an external incompressibility constraint to our model is related to the model itself: the main advantage of the St Venant-Kirchhoff model is to use the strain tensor E which is invariant with respect to rotations. But it is also invariant with respect to symmetries, which could lead to the reversal of some tetrahedra under strong constraints.

We choose to penalize volume variation by applying to each vertex of the tetrahedron a force directed along the normal of the opposite face $\mathbf{N}_p$ (see figure on the right), the norm of the force being the square of the relative volume variation:

$$\mathbf{F}_{incomp}^p = \left(\frac{V - V_0}{V_0}\right)^2 \vec{\mathbf{N}}_p.$$

These forces act as a pressure increase inside the tetrahedron. This method is closely related to Lagrange multipliers, which are often used to solve problem of energy minimization under constraints.

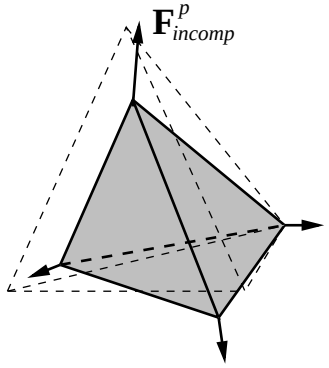

Figure 4: *Penalization of the volume variation*

5 Results

In the first experiment, we wish to highlight the contributions of our new deformable model in the case of partial rotations. Figure 5 shows the same experience as the one presented for linear elasticity (section 2.2, figure 3). On the left we can see that the cylinder vertices can now follow trajectories different from straight lines (figure 5(a)), leading to much more realistic deformations than in the linear (wire-frame) case (figures 5(b) and 5(c)).

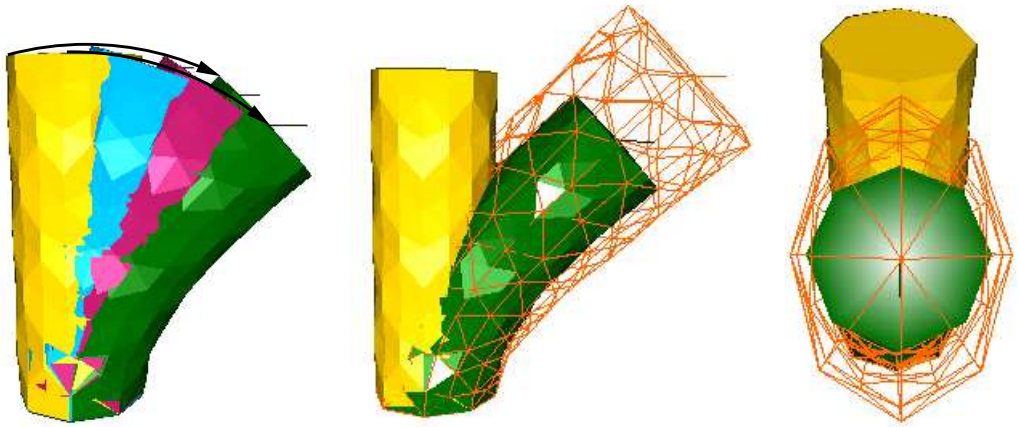

(a) (b) (c)

Figure 5: *(a) Successive deformations of the non-linear model. Side (b) and top (c) view of the comparison between linear (wire-frame) and non-linear model (solid rendering)*

The second example presents the differences between isotropic and anisotropic materials. The three cylinders of figure 6 have their top and bottom faces fixed, and are submitted to the same forces. While the isotropic model on the left undergoes a "snake-like" deformation, the last two, which are anisotropic along their height, stiffen in order to minimize their stretch in the anisotropic direction. The rightmost model, being twice as stiff as the middle one in the anisotropic direction, starts to squeeze in the plane of isotropy because it can not stretch anymore.

In the third example (figure 7), we apply a force to the right lobe of the liver (the liver is fixed in a region near the center of its back side, and Lamé constants are: $\lambda = 4.10^4 kg/cm^2$ and $\mu = 10^4 kg/cm^2$). Using the linear model, the right part of the liver undergoes a large (and unrealistic) volume increase, whereas with non-linear elasticity, the right lobe is able to partially rotate, while undergoing a much more realistic deformation.

Adding the incompressibility constraint on the same examples decreases the volume variation even more (see table 2), and also stabilizes the behaviour of the deformable models in strongly constrained areas.

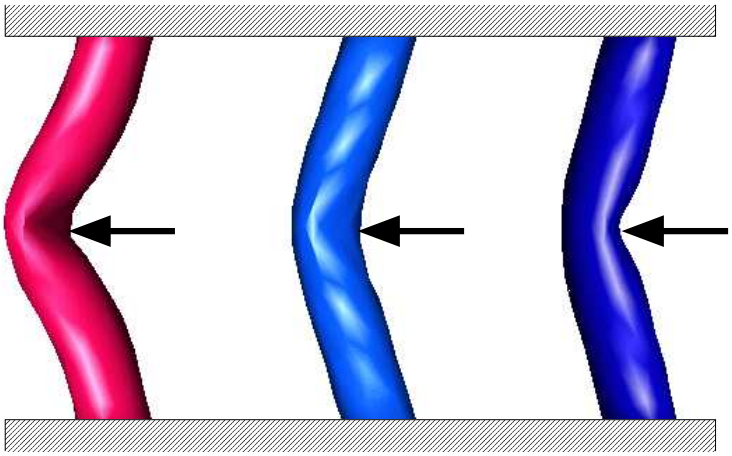

$\lambda = 2.10^5\ kg/cm^2$	$\lambda = 2.10^5\ kg/cm^2$	$\lambda = 2.10^5\ kg/cm^2$
$\mu = 10^5\ kg/cm^2$	$\mu = 10^5\ kg/cm^2$	$\mu = 10^5\ kg/cm^2$
-	$\lambda^L = 10^6\ kg/cm^2$	$\lambda^L = 2.10^6\ kg/cm^2$
-	$\mu^L = 5.10^5\ kg/cm^2$	$\mu^L = 10^6\ kg/cm^2$

Figure 6: *Deformation of tubular structures with non-linear transversally isotropic elasticity.*

Volume variations (%)	Linear	Non-linear	Non-linear incomp.
Cylinder **left** | **middle** | **right**	7 | 28 | 63	0.3 | 1 | 2	0.2 | 0.5 | 1
Liver	9	1.5	0.7

Table 2: *Volume variation results. For the cylinder: left, middle and right stand for the different deformations of figures 3 and 5(a)*

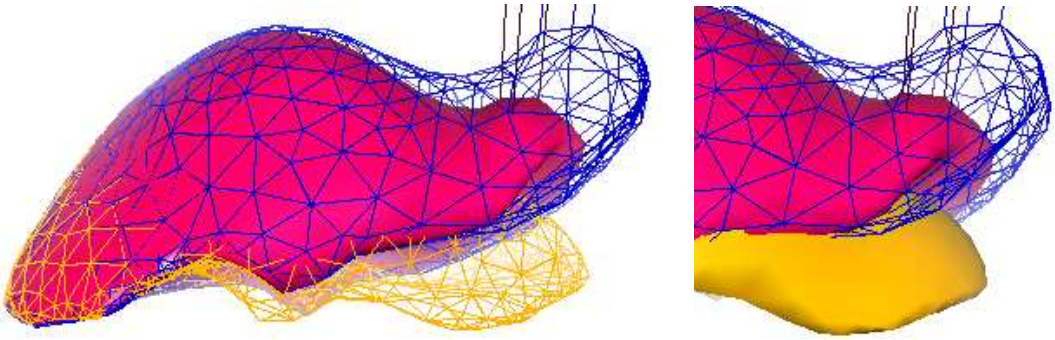

Figure 7: *Linear (wireframe), non-linear (solid) liver models, and rest shape (bottom)*

The last example is the simulation of a typical laparoscopic surgical gesture on the liver. One tool is pulling the edge of the liver sideways while a bipolar cautery device cuts it. During the cutting, the surgeon pulls away the part of the liver he wants to remove. This piece of liver undergoes large displacements and the deformation appears fairly realistic with this new non-linear deformable model (figure 8).

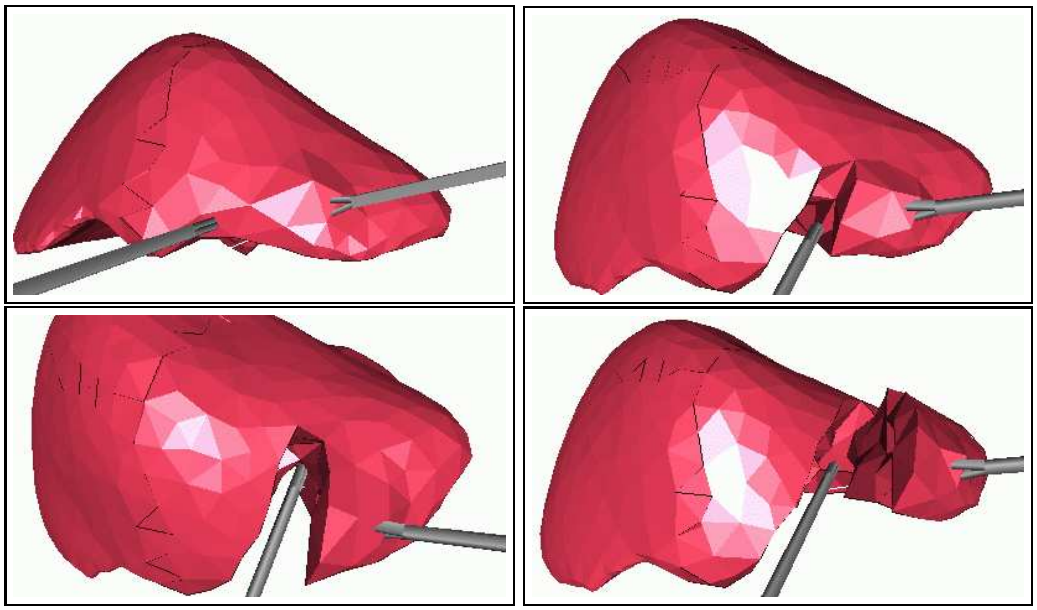

Figure 8: *Simulation of laparoscopic liver surgery*

Obviously, the computation time of this model is larger than for the linear model because the force equation is much more complex (equation 9). With our current implementation, simulation frequency is five times slower than with the linear model. Nevertheless, with this non-linear model, we can reach a frequency update of 25 Hz on meshes made of about 2000 tetrahedra (on a PC Pentium PIII 500M Hz). This is sufficient to reach visual real-time with quite complex objects, and even to provide a realistic haptic feedback using force extrapolation as described in [17].

6 Optimization of non-linear deformations

We have shown in this article that non-linear elasticity allows us to simulate much more realistic deformations than linear elasticity as soon as the model undergoes large displacements. However, non-linear elasticity is more computationally expensive than linear elasticity. Since non-linear elastic forces tend to linear elastic forces as the maximum vertex displacement decreases to zero, we propose to use non-linear elasticity only at parts of the mesh where displacements are larger than a given threshold, the remaining part using linear elasticity. Thus, we have modified the force computation algorithm in the following manner: for each vertex, we first compute the linear part of the force, and we add the non-linear part only if its displacement is larger than a threshold.

Figure 9 shows a deformation computed with this optimization (same model as in figure 7). This liver model is made of 6342 tetrahedra and 1394 vertices. The threshold is set to 2 cm while the mesh is about 30 cm long. The points drawn on the surface identify vertices using non-linear elasticity. With this method, we reach an updating frequency of 20 Hz instead of 8 Hz with a fully non-linear model. The same deformation is presented on

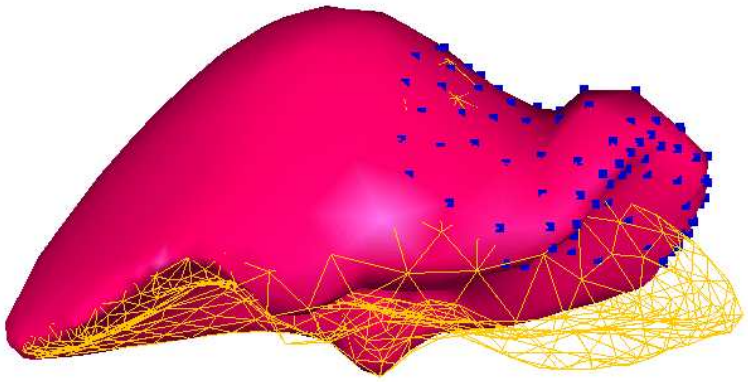

Figure 9: *Adaptable non-linear model deformation compared with its rest position (wire-frame)*

figure 10 for different values of the threshold. With this method, we can choose a trade-off between the bio-mechanical realism of the deformation and the updating frequency of the simulation.

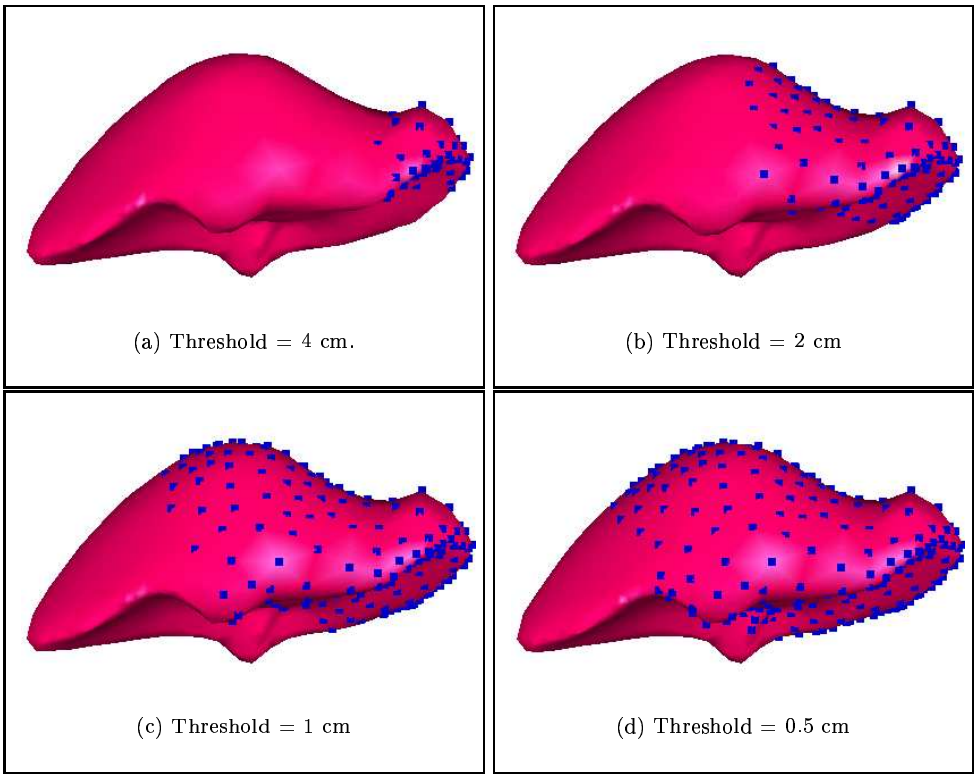

(a) Threshold = 4 cm. (b) Threshold = 2 cm

(c) Threshold = 1 cm (d) Threshold = 0.5 cm

Figure 10: *Deformation of the adaptable non-linear model for several values of the threshold.*

The diagram below shows the updating frequencies reached for each value of the threshold, in comparison with the fully linear and the fully non-linear models. Even when the threshold tends towards infinity, the adaptable model is slower than the linear model, because the computation algorithm of the non-linear force is more complex. Indeed, the computation of non-linear forces requires to visit all vertices, edges, triangles, and tetrahedra of the mesh, whereas only vertices and edges need to be visited for the linear model.

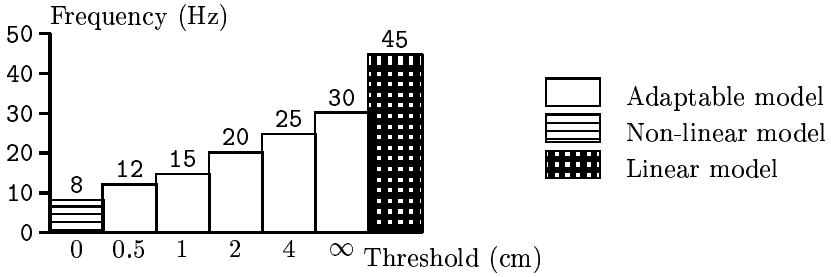

For the simulation example of figure 8, this optimization allows to reach updating frequencies varying between 50 and 80 Hz, depending on the ratio of points using non-linear elasticity (figure 11). The minimal frequency of 50 Hz is reached at the end of the simulation, when all vertices of the resected part of the liver are using large displacement elasticity (on the right of figure 11).

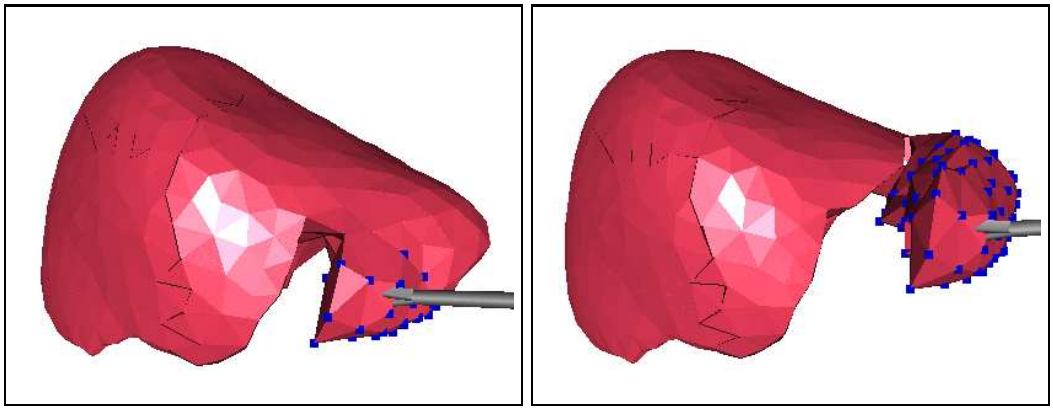

Figure 11: *Surgery simulation using adaptable model*

7 Validation

The liver is filled with blood (near 50% of its global weight), which implies that ex-vivo liver tissues should not behave like in-vivo tissues. Therefore, to validate our biomechanical liver model, we would have to compare it against in-vivo deformations of a real liver. Currently, such an experiment raises several technical and ethical difficulties. For the same reasons, the elastic properties of the liver (Young modulus and Poison ratio) must be measured in-vivo, or using complex in-vitro experimental protocols. In both cases, the results obtained by several teams (F. Carter *et al.* [5], V. Vuskovic [21], D. Dan [9]) have shown a strong variability in the parameters estimation.

In the framework of real-time surgery simulation, we essentially need to build soft tissue models that behave realistically. Therefore, we are currently relying on the feedback from surgeons experimenting the simulator to validate the behavior of our liver model. They consider that this St Venant-Kirchhoff non-linear elastic modeling of soft tissues is sufficient for most simulation purposes.

8 Conclusion

We have proposed in this article a new deformable model based on large displacement elasticity, a finite element method, and a dynamic explicit integration scheme. It solves the problem of rotational invariance and takes into account the anisotropic behavior and the incompressibility properties of biological tissues. Furthermore we have optimized the computation time of this model by computing the non-linear part of the force only for the parts of the mesh which undergo "large displacements".

Including this model into our laparoscopic surgery simulator prototype improves its biomechanical realism and thus increases its potential use for learning and training processes.

Our future work will focus on improving the computation efficiency with a new formulation of large displacement elasticity. Also, we plan to include vessels networks inside hepatic parenchyma and introduce, besides our geometric and physical models, a preliminary physiological model.

A Update operations when removing a tetrahedron from the mesh

When we remove a tetrahedron form the mesh, we need to update stiffness parameters of 4 vertices, 6 edges, and 4 faces, which means 280 floating number operations (see table 1):

$$
\begin{aligned}
& 4 * (1 \text{ tensor} + 1 \text{ vector} + 1 \text{ scalar}) \\
+\ & 6 * (1 \text{ tensor} + 4 \text{ vectors} + 5 \text{ scalars}) \\
+\ & 4 * (3 \text{ vectors} + 9 \text{ scalars}) \\
=\ & 280 \text{ real numbers}
\end{aligned}
$$

B Non-linear force equation

Equation 9 gives the force applied by tetrahedron $\mathbf{T}_i$ on vertex $\mathbf{P}_p$. To build the corresponding tensor-mass model, we need to split this equation (i.e. to split the sums) into different forces, respectively computed on vertex $\mathbf{P}_p$, on edges $(\mathbf{P}_p, \mathbf{P}_j)$, on triangles $(\mathbf{P}_p, \mathbf{P}_j, \mathbf{P}_k)$, and the tetrahedron $\mathbf{T}_i$. Then, we add the contributions of all adjacent tetrahedra, to obtain the equation which gives the force applied on vertex $\mathbf{P}_p$ as a function of the displacements

of its neighbors:

$$
\begin{aligned}
\mathbf{F}^p \;=\; & \boxed{\begin{array}{l}\text{Vertex contribution}\\ \\ 2\left[\mathcal{B}^{pp}\right]\mathbf{U}_p \\ +\;\left[2\left(\mathbf{U}_p\otimes\mathbf{U}_p\right)+\left(\mathbf{U}_p.\mathbf{U}_p\right)Id_3\right]\mathcal{C}^{ppp} \\ +\;4\mathcal{D}^{pppp}\;\mathbf{U}_p\;\mathbf{U}_p^t\;\mathbf{U}_p\end{array}} \\
+ & \sum_{edges(p,j)} \boxed{\begin{array}{l}\text{Edge contribution}\\ \\ 2\left[\mathcal{B}^{pj}\right]\mathbf{U}_j \\ +\;2\left[\left(\mathbf{U}_j\otimes\mathbf{U}_p\right)+\left(\mathbf{U}_j.\mathbf{U}_p\right)Id_3\right]\mathcal{C}^{ppj}+2\left(\mathbf{U}_p\otimes\mathbf{U}_j\right)\mathcal{C}^{jpp} \\ \quad +2\left(\mathbf{U}_j\otimes\mathbf{U}_j\right)\mathcal{C}^{jjp}+\left(\mathbf{U}_j.\mathbf{U}_j\right)\mathcal{C}^{pjj} \\ +\;4\left[\mathcal{D}^{jppp}\;\left(2\mathbf{U}_p\;\mathbf{U}_p^t\;\mathbf{U}_j+\mathbf{U}_j\;\mathbf{U}_p^t\;\mathbf{U}_p\right)+\mathcal{D}^{jjpp}\;\mathbf{U}_p\;\mathbf{U}_j^t\;\mathbf{U}_j\right. \\ \quad \left.+\left(\mathcal{D}^{jpjp}+\mathcal{D}^{pjjp}\right)\mathbf{U}_j\;\mathbf{U}_j^t\;\mathbf{U}_p+\mathcal{D}^{jjjp}\;\mathbf{U}_j\;\mathbf{U}_j^t\;\mathbf{U}_j\right]\end{array}} \\
+ & \sum_{faces(p,j,k)} \boxed{\begin{array}{l}\text{Face contribution}\\ \\ 2\left[\left(\mathbf{U}_k\otimes\mathbf{U}_j\right)\mathcal{C}^{jkp}+\left(\mathbf{U}_j\otimes\mathbf{U}_k\right)\mathcal{C}^{kjp}+\left(\mathbf{U}_j.\mathbf{U}_k\right)\mathcal{C}^{pjk}\right] \\ +\;4\left[\left(\mathcal{D}^{pjkp}+\mathcal{D}^{jpkp}\right)\left(\mathbf{U}_j\;\mathbf{U}_k^t\;\mathbf{U}_p+\mathbf{U}_k\;\mathbf{U}_j^t\;\mathbf{U}_p\right)+2\mathcal{D}^{jkpp}\;\mathbf{U}_p\;\mathbf{U}_j^t\;\mathbf{U}_k\right. \\ \quad +\left(\mathcal{D}^{kjjp}+\mathcal{D}^{jkjp}\right)\mathbf{U}_j\;\mathbf{U}_j^t\;\mathbf{U}_k+\mathcal{D}^{jjkp}\;\mathbf{U}_k\;\mathbf{U}_j^t\;\mathbf{U}_j \\ \quad \left.+\left(\mathcal{D}^{jkkp}+\mathcal{D}^{kjkp}\right)\mathbf{U}_k\;\mathbf{U}_k^t\;\mathbf{U}_j+\mathcal{D}^{kkjp}\;\mathbf{U}_j\;\mathbf{U}_k^t\;\mathbf{U}_k\right]\end{array}} \\
+ & \sum_{tetra(p,j,k,l)} \boxed{\begin{array}{l}\text{Tetrahedron contribution}\\ \\ 4\left[\left(\mathcal{D}^{jklp}+\mathcal{D}^{kjlp}\right)\mathbf{U}_l\;\mathbf{U}_j^t\;\mathbf{U}_k+\left(\mathcal{D}^{jlkp}+\mathcal{D}^{ljkp}\right)\mathbf{U}_k\;\mathbf{U}_j^t\;\mathbf{U}_l\right. \\ \quad \left.+\left(\mathcal{D}^{kljp}+\mathcal{D}^{lkjp}\right)\mathbf{U}_j\;\mathbf{U}_k^t\;\mathbf{U}_l\right]\end{array}}
\end{aligned}
$$

References

[1] N. Ayache, S. Cotin, H. Delingette, J.-M. Clement, J. Marescaux, and M. Nord. Simulation of endoscopic surgery. *Journal of Minimally Invasive Therapy and Allied Technologies (MITAT)*, 7(2):71–77, July 1998.

[2] C. Basdogan, C. Ho, M. A. Srinivasan, S. D. Small, and S. L. Dawson. Force Interaction in Laparoscopic Simulation: Haptic Rendering Soft Tissues. In *Medecine Meets Virtual Reality (MMVR'6)*, pages 28–31, San Diego CA, january 1998.

[3] K.-L. Bathe. *Finite Element Procedures in Engineering Analysis.* Prentice-Hall, 1982.

[4] Morten Bro-Nielsen and Stephane Cotin. Real-time Volumetric Deformable Models for Surgery Simulation using Finite Elements and Condensation. In *Eurographics '96. ISSN 1067-7055*, pages 57–66. Blackwell Publishers, 1996.

[5] F. J. Carter. Biomechanical testing of intra-abdominal soft tissue. In *International Workshop on Soft Tissue Deformation and Tissue Palpation*, Cambridge, MA, October 1998.

[6] P. G. Ciarlet. *Mathematical elasticity Vol. 1: Three-dimensional elasticity.* Elsevier Science Publishers B.V., 1988.

[7] S. Cotin, H. Delingette, and N. Ayache. Real-time elastic deformations of soft tissues for surgery simulation. *IEEE Transactions On Visualization and Computer Graphics*, 5(1):62–73, January-March 1999.

[8] S. Cotin, H. Delingette, and N. Ayache. A Hybrid Elastic Model allowing Real-Time Cutting, Deformations and Force-Feedback for Surgery Training and Simulation. *The Visual Computer*, 2000. to appear (see INRIA research report RR-3510).

[9] D. Dan. *Caractérisation mécanique du foie humain en situation de choc.* PhD thesis, Université Paris 7, September 1999.

[10] F. Boux de Casson and C. Laugier. Modeling the Dynamics of a Human Liver for a Minimally Invasive Surgery Simulator. In *MICCAI'99*, Cambridge UK, 1999.

[11] G. Debunne, M. Desbrun, A. Barr, and M.-P. Cani. Interactive multiresolution animation of deformable models. In *10th Eurographics Workshop on Computer Animation and Simulation (CAS'99)*, September 1999.

[12] H. Delingette, S.Cotin, and N.Ayache. A Hybrid Elastic Model allowing Real-Time Cutting, Deformations and Force-Feedback for Surgery Training and Simulation. In *Computer Animation*, Geneva, Switzerland, May 26-28 1999.

[13] Y. C. Fung. *Biomechanics - Mechanical Properties of Living Tissues.* Springer-Verlag, second edition edition, 1993.

[14] D. Lamy and C. Chaillou. Design, Implementation and Evaluation of an Haptic Interface for Surgical Gestures Training. In *International Scientific Workshop on Virtual Reality and Prototyping*, pages 107–116, Laval, France, June 1999.

[15] J. Marescaux, J-M. Clément, V. Tassetti, C. Koehl, S. Cotin, Y. Russier, D. Mutter, H. Delingette, and N. Ayache. Virtual Reality Applied to Hepatic Surgery Simulation: The Next Revolution. *Annals of Surgery*, 228(5):627–634, 1998.

[16] W. Maurel, Y. Wu, N. M. Thalmann, and D. Thalmann. *Biomechanical Models for Soft Tissue Simulation.* Springer-Verlag, 1998.

[17] G. Picinbono, J.C. Lombardo, H. Delingette, and N. Ayache. Anisotropic Elasticity and Force Extrapolation to Improve Realism of Surgery Simulation. In *IEEE International Conference on Robotics and Automotion: ICRA 2000*, pages 596–602, San Francisco, CA, April 2000.

[18] G. Picinbono, J.C. Lombardo, H. Delingette, and N. Ayache. Improving Realism of a Surgery Simulator: Linear Anisotropic Elasticity, Complex Interactions and Force Extrapolation. Technical report, INRIA, October 2000.

[19] G. Székely, M. Bajka, C. Brechbuhler, J. Dual, R. Enzler, U. Haller, J. Hug, R. Hutter, N. Ironmonger, M. Kauer, V. Meier, P. Niederer, A. Rhomberg, P. Schmid, G. Schweitzer, M. Thaler, V. Vuskovic, and G. Troster. Virtual Reality Based Simulation of Endoscopic Surgery. *Presence, MIT press*, 9(3):310–333, June 2000.

[20] G. Székely, Ch. Brechbühler, R. Hutter, A. Rhomberg, and P. Schmid. Modelling of soft tissue deformation for laparoscopic surgery simulation. *Medical Image Analysis*, 4:57–66, 2000.

[21] V. Viskovic, M. Kauer, G. Székely, and M. Reidy. Realistic Force Feedback for Virtual Reality Based Diagnostic Surgery Simulators. In *IEEE International Conference on Robotics and Automotion: ICRA 2000*, pages 1592–1598, San Francisco, CA, April 2000.

[22] O. Zienkiewics. *The finite element method.* Mc Graw-Hill, London, 3^{rd} edition, 1977.

Unité de recherche INRIA Sophia Antipolis
2004, route des Lucioles - B.P. 93 - 06902 Sophia Antipolis Cedex (France)

Unité de recherche INRIA Lorraine : Technopôle de Nancy-Brabois - Campus scientifique
615, rue du Jardin Botanique - B.P. 101 - 54602 Villers lès Nancy Cedex (France)
Unité de recherche INRIA Rennes : IRISA, Campus universitaire de Beaulieu - 35042 Rennes Cedex (France)
Unité de recherche INRIA Rhône-Alpes : 655, avenue de l'Europe - 38330 Montbonnot St Martin (France)
Unité de recherche INRIA Rocquencourt : Domaine de Voluceau - Rocquencourt - B.P. 105 - 78153 Le Chesnay Cedex (France)

Éditeur
INRIA - Domaine de Voluceau - Rocquencourt, B.P. 105 - 78153 Le Chesnay Cedex (France)
http://www.inria.fr
ISSN 0249-6399